ARTICLES
https://doi.org/10.1038/s41928-020-0402-3

nature electronics

Extraordinary performance of semiconducting metal oxide gas sensors using dielectric excitation

Radislav A. Potyrailo[1]✉, Steven Go[1], Daniel Sexton[1], Xiaxi Li[2], Nasr Alkadi[3], Andrei Kolmakov[4], Bruce Amm[1], Richard St-Pierre[1], Brian Scherer[1], Majid Nayeri[1], Guang Wu[1], Christopher Collazo-Davila[1], Doug Forman[1], Chris Calvert[5], Craig Mack[5] and Philip McConnell[5]

Semiconducting metal oxides are widely used for gas sensors. The resulting chemiresistor devices, however, suffer from non-linear responses, signal fluctuations and gas cross-sensitivities, which limits their use in demanding applications of air-quality monitoring. Here, we show that conventional semiconducting metal oxide materials can provide high-performance sensors using an impedance measurement technique. Our approach is based on dielectric excitation measurements and yields sensors with a linear gas response ($R^2 > 0.99$), broad dynamic range of gas detection (six decades of concentrations) and high baseline stability, as well as reduced humidity and ambient-temperature effects. We validated the technique using a range of commercial sensing elements and a range of gases in both laboratory and field conditions. Our approach can be applied to both n- and p-type semiconducting metal oxide materials, and we show that it can be used in wireless sensor networks, and drone-based and wearable environmental and industrial gas monitoring.

Modern gas sensors are capable of operating at a low power and have a low cost, and can be used in a range of applications[1–7]. Sensors based on semiconducting metal oxide (SMOX) materials, which rely on changes in electrical resistance (chemiresistors), are used in a variety of practical settings[8,9], which include air-quality alarms for residential, industrial and automotive applications. In such implementations, the performance limitations of SMOX sensors, which include non-linearity, poor stability and gas cross-sensitivity, are not critical. However, these limitations make the sensors unsuitable for other contemporary monitoring needs, such as the reliable monitoring of ambient environmental pollutants and indoor air quality, and the surveillance of hazardous industrial areas.

To reduce the gas cross-sensitivity of SMOX-based sensors, several approaches have been employed: combining sensors into arrays, using temperature modulation to improve the sensor response and broad-range impedance spectroscopy (Supplementary Notes 1–3). In particular, platforms based on sensor arrays and temperature modulation are currently close to field implementation[10–12]. The non-linearity of SMOX sensors, however, has been assumed to be an inherent issue due to the power law that governs their d.c. resistance response[13–20]. The non-linear response degrades the sensitivity of SMOX sensors at high gas concentrations[21] and makes additional sensor calibration necessary[6], which increases costs. Finally, the issue of poor operation stability[22] degrades the limit of detection (LOD) of the sensors.

In this article, we show that gas sensors based on SMOX materials can yield a linear response by using impedance measurements based on a dielectric excitation technique. In particular, the imaginary part of the a.c. impedance at a certain frequency range can provide a linear sensor response over a large range of gas concentrations. Also, compared to conventional chemiresistors, our approach expands the dynamic range of gas detection, improves sensor baseline stability, and significantly reduces, or even eliminates, humidity and ambient temperature effects. Unlike broad-band impedance spectroscopy, our dielectric excitation approach uses specific frequency ranges by following the front (high- or low-frequency) shoulder of the spectral peak obtained from dielectric relaxation measurements of (n- or p-type, respectively) SMOX materials when they are exposed to various gas concentrations.

We first used the SnO_2 SMOX material, which is an n-type semiconductor and is the most popular material in SMOX sensors[8,9]. We then validated our measurement strategy using 15 different sensing elements and numerous gaseous species at different concentration ranges. A broad range of volatiles of environmental and industrial importance were tested: benzene, toluene, hydrogen sulfide, hydrogen, carbon monoxide, methane, ethane, propane, acetylene, methanol, ethanol, acetone and formaldehyde. We also explored the effects of humidity (mixtures of volatiles with water vapour up to 80% relative humidity (RH)) and temperature (−25 to 50 °C). Furthermore, we applied our dielectric excitation measurement strategy to a p-type SMOX material and confirmed the same response linearity. For both n- and p-type SMOX materials, we employed sensing elements fabricated by state-of-the-art manufacturing practices (Fig. 1a and Supplementary Table 1) rather than custom structures that may have non-Debye contributions to their response. To illustrate the practical potential of our strategy, we built wireless sensor nodes using low-power microelectronics and employed them for stationary, drone-based and wearable environmental and industrial gas monitoring.

Response linearity with diverse sensing elements and gases

The power law in SMOX chemiresistors originates from the gas-induced changes in the electrical conduction and polarization effects along the percolating conduction paths of the sensing material[16]. These paths are the individual grains, as well as the interconnects between the grains and the contacts with electrodes (Fig. 1b,c), as described by a widely accepted equivalent circuit

[1]GE Global Research, Niskayuna, NY, USA. [2]GE Global Growth Organization, Shanghai, China. [3]BHGE Oil & Gas Technology Center, Oklahoma, OK, USA. [4]National Institute of Standards and Technology, Gaithersburg, MD, USA. [5]GE Renewable Energy, Lisburn, Ireland. ✉e-mail: potyrailo@ge.com

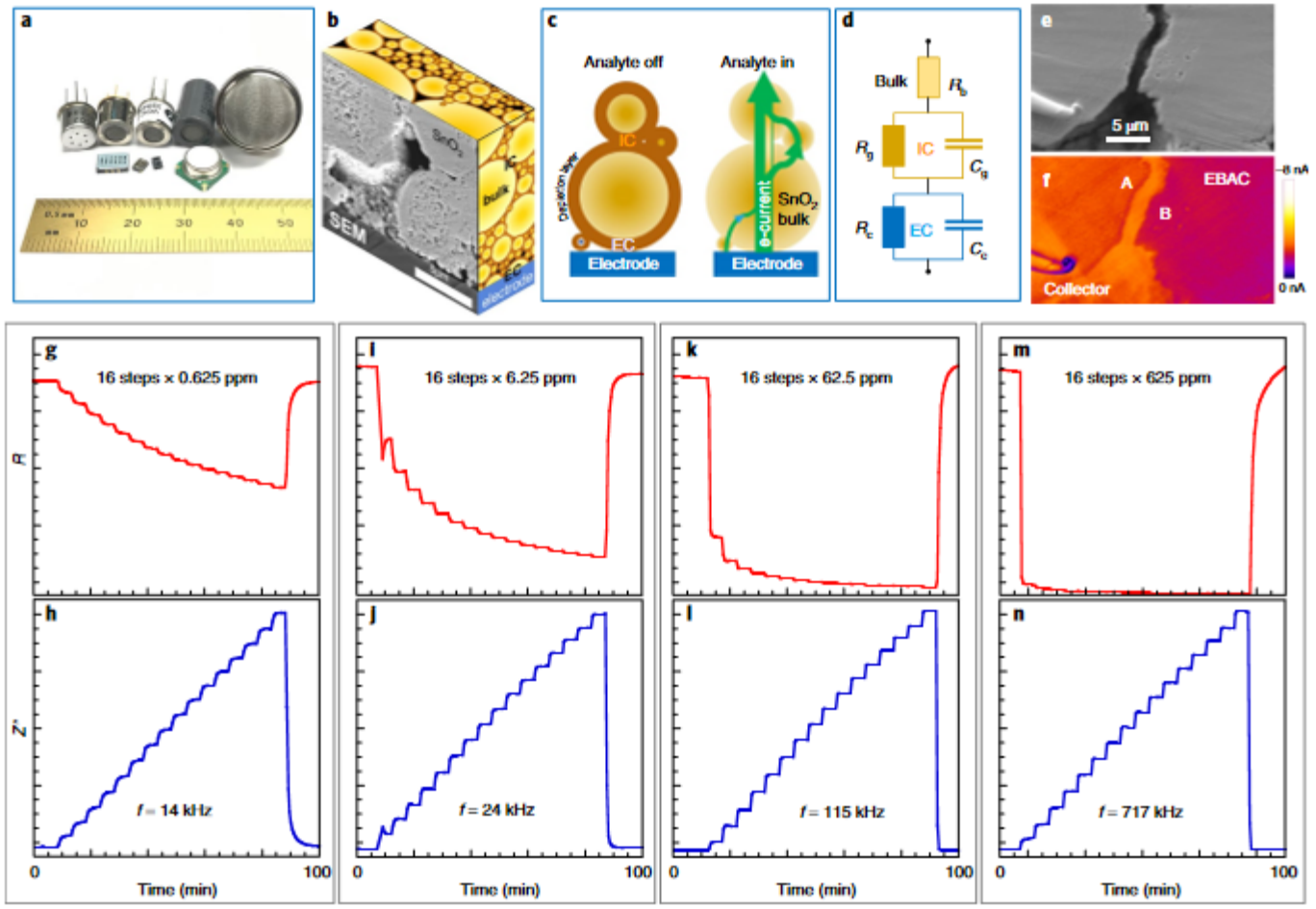

Fig. 1 | Metal oxide semiconducting materials for gas sensing using conventional resistance and dielectric excitation schemes. a, Examples of SMOX sensing elements fabricated by high-quality manufacturing practices. SMOX sensing materials are deposited between or on top of electrodes on heated substrates. **b**, Cross-sectional scanning electron microscope (SEM) image of the SnO_2 sensing material in contact with an electrode with its visualized hierarchical granular and porous structure. **c**, The mechanism of gas sensitivity of SnO_2 in which a gas-induced SnO_2 band bending causes the modulation of the electrical conduction and polarizing effects at intergranular contacts (ICs), electrode/particle contacts (ECs), grain and bulk boundaries and the bulk resistance of grains. **d**, The equivalent circuit diagram in which an EC has resistance R_c and capacitance R_c, the IC has resistance R_g and capacitance C_g, and R_b is the bulk resistance of the core of the grains. **e**,**f**, In situ SEM electrical characterization (**e**) and EBAC current collection (**f**) map the SnO_2 sensing material. The colour contrast is determined mainly by the absorbed current; the gradual variation of the colour scale along the individual contacted grains A and B indicates that the conductance in the bulk is ohmic. The step-like difference in the colour level between grains A and B shows the presence of a potential barrier between them. **g**–**n**, Monitoring of different concentration ranges of methane using conventional resistance (**g**,**i**,**k**,**m**) and dielectric excitation (**h**,**j**,**l**,**n**) measurements using a sensing element TGS 2611: 0–10 ppm (**g**,**h**), 0–100 ppm (**i**,**j**), 0–1,000 ppm (**k**,**l**) and 0–10,000 ppm (**m**,**n**). For each concentration range, 16 steps of gas concentrations were produced. Dielectric excitation Z'' measurements were at 14 kHz, 24 kHz, 115 kH and 717 kHz for **h**, **j**, **l** and **n**, respectively.

model (Fig. 1d). The conductance in the SMOX bulk material follows an ohmic behaviour with a potential barrier between grains, as determined using electron beam absorbed current (EBAC) microscopy (Fig. 1e,f).

For our initial experiments, we used a commercial methane sensing element (TGS 2611) and tested it with methane as a model greenhouse gas at various ppb and ppm levels, as well as a model flammable gas at various volume percent levels. From measurements of the real $Z'(f)$ and imaginary $Z''(f)$ impedance at different frequencies f, we found that the $Z''(f)$ response to the gas exhibited linearity at certain frequencies (at the high-frequency shoulder of the relaxation peak spectra). For example, for the measurements using 0–10 ppm of methane, the resistance response showed a non-linear behaviour (Fig. 1g), whereas the Z'' (f) response became linear with the coefficient of determination $R^2 > 0.995$ at the high-frequency shoulder of the dielectric relaxation region (Fig. 1h). We observed this linear behaviour up to the highest methane concentration of 10,000 ppm allowed in ambient laboratory conditions but the resistance response progressively saturated (Fig. 1g–n and Extended Data Fig. 1).

These results were intriguing because decades of prior work on impedance spectroscopy of SMOX sensing materials did not report such linear response (Supplementary Note 3). To understand the mechanism of such responses of a conventional SnO_2 material when using the dielectric excitation measurements, we considered a SMOX material as a condensed-phase material with a response to a gas. In this material, the dielectric relaxation region is controlled by the circuit resistance R and capacitance C (ref. [23]). As an approximation, we considered the exposure of the material to a single type of gas at different concentrations, the circuit resistance R to follow the classic empirical power law response on gas exposures[13–20] and the circuit capacitance C to be constant because the gas effects on

the capacitance of SnO_2 sensors are relatively small[24,25]. In materials science, $Z'(f)$ and $Z''(f)$ dispersion profiles are measured to extract material properties (Supplementary Note 4) given by:

$$Z' = \frac{R}{1 + (2\pi f C R)^2} \quad (1)$$

$$Z'' = \frac{-R^2 C 2\pi f}{1 + (2\pi f C R)^2} \quad (2)$$

According to equation (1), at $f \to 0$, a condensed-phase material exhibits a high value of Z', which is equal to R, followed by a gradual relaxation of $Z'(f)$ to zero as a function of frequency. According to equation (2), a relaxation peak exists in the $Z''(f)$ spectrum with its minimum at the relaxation frequency f_o. The $Z''(f)$ spectrum also exhibits a relaxation to zero as a function of frequency. If this condensed-phase material is a gas-sensitive metal oxide, its resistance R follows the classic empirical power-law response with gas exposures[13–20]. To describe the resistor response at different concentrations of an analyte gas [gas], which includes when [gas] = 0, the power law can be expressed as:

$$R = R_o\left(1 + K_{gas}[\text{gas}]\right)^{-\beta} \quad (3)$$

where R_o is the material resistance in the absence of analyte gas, K_{gas} is the resistance sensitivity to the analyte gas and β is the power-law coefficient of response. Numerous previous studies showed that the coefficient K_{gas} depends on the nature of the gas, type of sensing material and sensor operating temperature, whereas the power-law exponent β depends on three categories of factors, (1) the nature of the measured gas and its concentration range, (2) the type of sensing material, its grain size, grain surface-to-volume ratio, types of dopants and types of interconnects between the grains and (3) the geometry and material of the electrodes of the sensing element[13–20].

To verify experimental results in Fig. 1g–n and Extended Data Fig. 1, we simulated the dispersion profiles $Z'(f)$ and $Z''(f)$ described by equations (1) and (2) and gas-induced changes in R described by equation (3). We visualized the linearity of theoretical and experimental responses across the dielectric relaxation region by normalizing $Z'(f)$ and $Z''(f)$ to be from 0 to 1 over the tested ranges of gas concentrations. The correlation between the theoretical and experimental results of normalized $Z'(f)$ and $Z''(f)$ is depicted in Fig. 2a–d and Supplementary Figs. 1 and 2. The normalized theoretical and experimental $Z'(f)$ responses followed the power law at low frequencies, becoming non-monotonic on frequency increase and monotonic at high frequencies, and did not become linear (Supplementary Fig. 1). The normalized theoretical and experimental $Z''(f)$ responses were non-linear at low frequencies, becoming more linear, slightly S-shaped and even exponential at high frequencies (Fig. 2a–d and Supplementary Fig. 2c,d). Such behaviour was from contributions of the gas-induced frequency shifts of the relaxation frequency f_o and the change in the $Z''(f)$ signal (see Initial design rules for high-linearity SMOX sensors).

To quantify the response linearity, we applied linear fits to the normalized $Z'(f)$ and $Z''(f)$ responses and calculated the R^2 values of these fits. A comparison of the R^2 values of the theorical and experimental $Z''(f)$ responses (Fig. 2e,f) shows a clear trend in the frequency positions that provided linear gas responses with the desired resolution. The linearity of the $Z''(f)$ responses was $R^2 > 0.995$ for theoretical and experimental values (Fig. 2e,f and Supplementary Fig. 3). This strong correlation between these initial theoretical and experimental $Z'(f)$ and $Z''(f)$ data (Fig. 2 and Supplementary Figs. 1–3) validated our initial model of the gas-response mechanism using dielectric excitation measurements. Theoretical and experimental data showed that the gas-response linearity of the condensed-phase n-type SMOX material was controlled by the measurement mode Z' or Z'' and frequency f as described by equations (1)–(3).

At very high measurement frequencies, the theoretical R^2 values stabilized (Fig. 2e), whereas the experimental R^2 values decreased and their noise increased (Fig. 2f). The insights of this discrepancy are provided from equations (1) and (2) and Extended Data Fig. 1, in which the $Z'(f)$ and $Z''(f)$ spectra gradually relax to zero as a function of frequency. Experimentally, these values approached the noise floor of the measurement system, so unable to resolve the gas response at high frequencies. In contrast, the simulations shown in Fig. 2e depict that in the absence of the measurement noise the response linearity was sustained at high frequencies. As shown in Figs. 1 and 2, with the extension of the gas concentration range, the best frequency to achieve the linear response increased. In measurements when the expected concentrations are unknown, the optimal frequency can be determined using known autoranging techniques (Supplementary Note 5 and Supplementary Fig. 4).

Our achieved control of response linearity with sensing of methane up to 10,000 ppm encouraged us to explore the potential of the dielectric excitation measurements to expand the dynamic range of gas detection even further. By testing the sensor response with 0.625-ppm steps of CH_4 concentration, we achieved a LOD of 20 ppb of methane (Extended Data Fig. 2a). Our tests with methane from 0 to 110,000 ppm (11% volume) in a special chemical hood also achieved a linear response (Extended Data Fig. 2b). Thus, we expanded the dynamic range of methane-gas sensing to more than six decades (5.5×10^6 fold). The response linearity over such a broad measurement range is an important milestone for SMOX sensing concepts because the power-law response of SMOX resistors limits the range down to typically 2–3 decades and rarely extends to 4 decades of gas concentrations[26].

We further compared the responses of our sensors with those of pellistors as established safety detectors of high levels of flammable gases. Supplementary Figs. 5 and 6 illustrate that our sensors were able to detect not only much lower concentrations of methane but also did not suffer from the erroneous decrease of pellistor response when detecting relatively high concentrations of methane. This broad range of measured gas concentrations opens the opportunities to monitor infrared-inactive industrial gases (for example, hydrogen) with complementary capabilities to those of pellistors.

To explore if the observed linear response with methane was common across diverse types of volatiles and designs of SMOX sensing elements, we tested 15 types of sensing elements with numerous volatiles. We selected SMOX sensing elements manufactured with bulk and thin-film structures and different configurations of electrodes (Supplementary Table 1). These sensing elements were with n-type, mostly SnO_2, material because it is the most popular SMOX material[8,9]. We utilized these sensing elements without any additional electronic circuit components (for example, potential dividers). In operation, the resistance of these sensing elements ranged from ~2×10^3 to 5×10^5 ohm. Diverse volatiles, such as hydrogen, carbon monoxide, methane, acetylene, methanol, ethanol, acetone, toluene, benzene, formaldehyde and hydrogen sulfide were measured because many of these chemical species were included in the specifications of SMOX chemiresistors driven by their dopants and by the importance for environmental and industrial applications.

Extended Data Fig. 3 and Supplementary Fig. 7 illustrate the results with these n-type SMOX sensing elements plotted as resistor and dielectric excitation responses. Using dielectric excitation methodology, we found linear response to numerous volatiles to be independent of the designs of the sensing elements and types of volatiles. Although most responses from diverse sensors were linear, some responses were slightly sigmoidal or had an enhanced sensitivity at high gas concentrations (Extended Data Fig. 3e and Supplementary Fig. 7e), as also theoretically and experimentally observed for methane (Supplementary Fig. 2c,d).

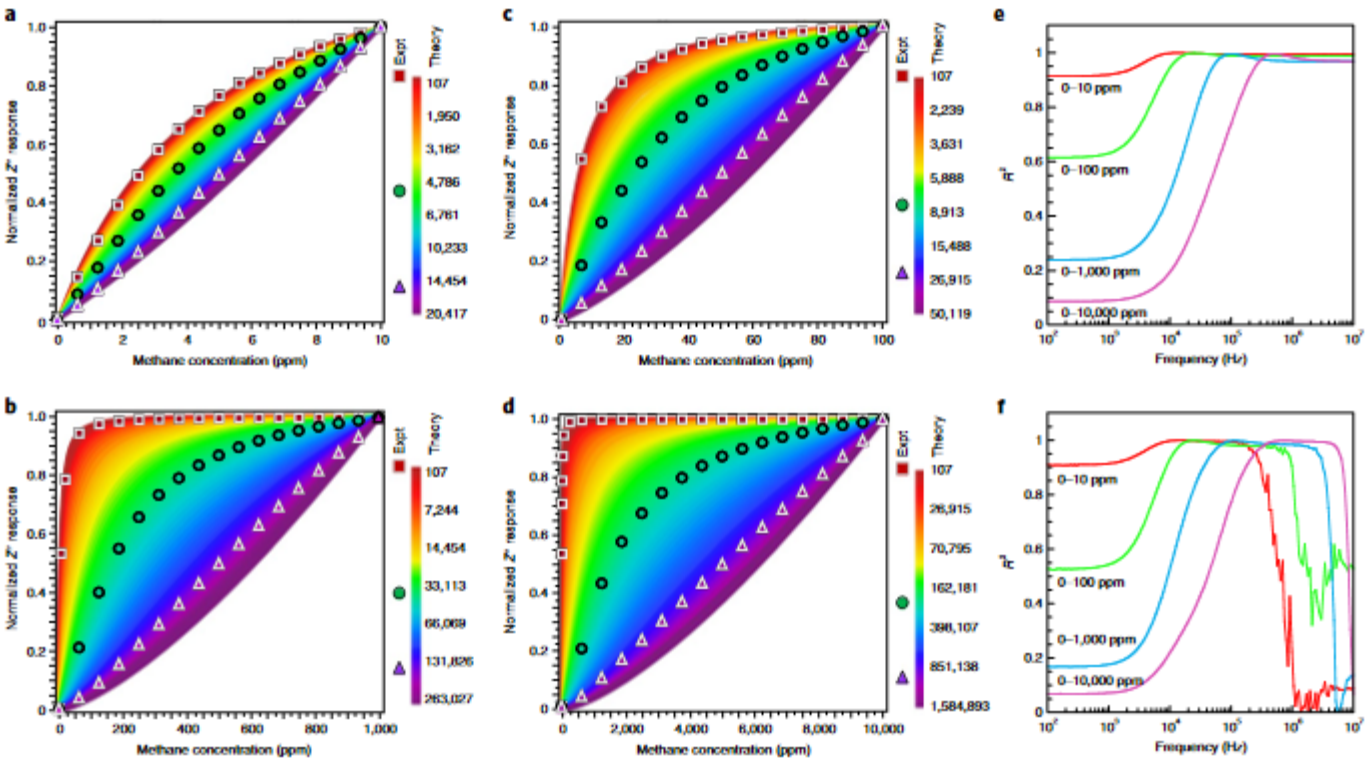

Fig. 2 | Theoretical verification of the experimentally developed dielectric excitation scheme for the controlled linearity of SMOX sensors. a–d, Normalized Z'' gas-response profiles to methane gas from 0 to 1 at various frequencies across the dielectric relaxation region of the SMOX sensing material at 0–10 ppm (**a**), 0–100 ppm (**b**), 0–1,000 ppm (**c**) and 0–10,000 ppm (**d**). The theoretical values are plotted as gradient colours. Exemplary sets of experimental data at three representative frequencies are shown with colours that correspond to the theoretical frequency values. **e**,**f**, Calculated R^2 values of linear fits to the theoretical (**e**) and experimental (**f**) $Z''(f)$ responses for all the measured concentration ranges of methane. Expt, experiment.

To investigate this phenomenon and to seek needed insights, we analysed these gas-response results as Nyquist plots (Supplementary Figs. 8 and 9). Although laboratory-prepared sensing materials can have Nyquist plots with almost ideal Debye relaxation[24,27], often in such manually prepared sensing materials there is also a substantial risk of having distorted Nyquist plots due to a variety of effects that cause non-Debye relaxation (Supplementary Note 3). The Nyquist plots from our tested sensing elements had zero depression angles of the Z' versus $-Z''$ semicircles that visualize no detected effects from non-Debye relaxation. The presence of only Debye relaxation in our Nyquist plots facilitated the development of our initial design rules for the sensors with a high response linearity based on the dielectric excitation strategy.

Encouraged by the gas-response linearity of n-type SMOX sensing elements, we tested a p-type SMOX sensing element (Supplementary Table 1) for its response to ethanol as a model analyte (Extended Data Fig. 4). In the case of the p-type SMOX material, the d.c. resistance increased with the increase of ethanol concentrations from ~2×10^5 ohm in air to ~3×10^6 ohm in ethanol following the power law; the $Z''(f)$ response was linear at the low-frequency shoulder of the relaxation peak (Extended Data Fig. 4a–d). The Nyquist plots had zero depression angles visualizing no detected effects from non-Debye relaxation (Extended Data Fig. 4e). The resulting $Z''(f)$ response at low frequencies had a linearity of $R^2=0.994$ (Extended Data Fig. 4f), similar to those of n-type SMOX materials.

Thus, for both, n- and p-type SMOX materials the linear $Z''(f)$ gas responses were observed on the front-edge shoulder of the relaxation peak that followed the gas concentrations. For n- and p-type materials, the front-edge shoulder was the high- or low-frequency regions of the relaxation peak, respectively as summarized in Extended Data Fig. 5.

Effects of variable ambient humidity and temperature

A variable air humidity affects the power-law response of chemiresistors by changing their baseline and gas sensitivity[28–31]. An example of the effects of water vapour from 0 to 80% RH on the resistance and dielectric responses to ethanol (as a model vapour) is presented in Fig. 3a–d. The resistance response had a known substantial decrease in baseline and decrease in gas sensitivity with the increase of RH (Fig. 3a,b shows the linear and logarithmic y scales, respectively). Meanwhile, the dielectric excitation provided three important advancements over the resistance measurements (Fig. 3c): (1) the response baseline was less affected by humidity variations, (2) the sensor sensitivity increased with the increase of RH and (3) the response linearity slightly improved in the presence of water vapour. We assessed the sensor linearity as R^2 values of the linear fit for dry air and four levels of RH (Fig. 3d) and had two additional findings: (1) R^2 increased with RH, from 0.975 (0% RH) to 0.997 (20% RH) and to 0.999 (80% RH) and (2) the frequency ranges of the linear response overlapped for 20–80% RH, being slightly lower for 0% RH. Thus, the dielectric excitation provided a linear response for different humidity levels, which simplifies the calibration of such sensors for practical uses[5].

We further performed additional studies of the RH effects on the linearity of diverse sensing elements and volatiles (Supplementary Figs. 10–15). We found that the response baseline was consistently less affected by humidity variations as compared to the resistance readout, the sensitivity of the sensors either increased or decreased with the increase of RH and the response linearity consistently improved with RH and had overlapping frequency ranges.

The effects of the ambient temperature on chemiresistors remain an unsolved problem that reduces sensor accuracy[32,33] and adds complications in sensor calibrations[5]. Dielectric excitation provided

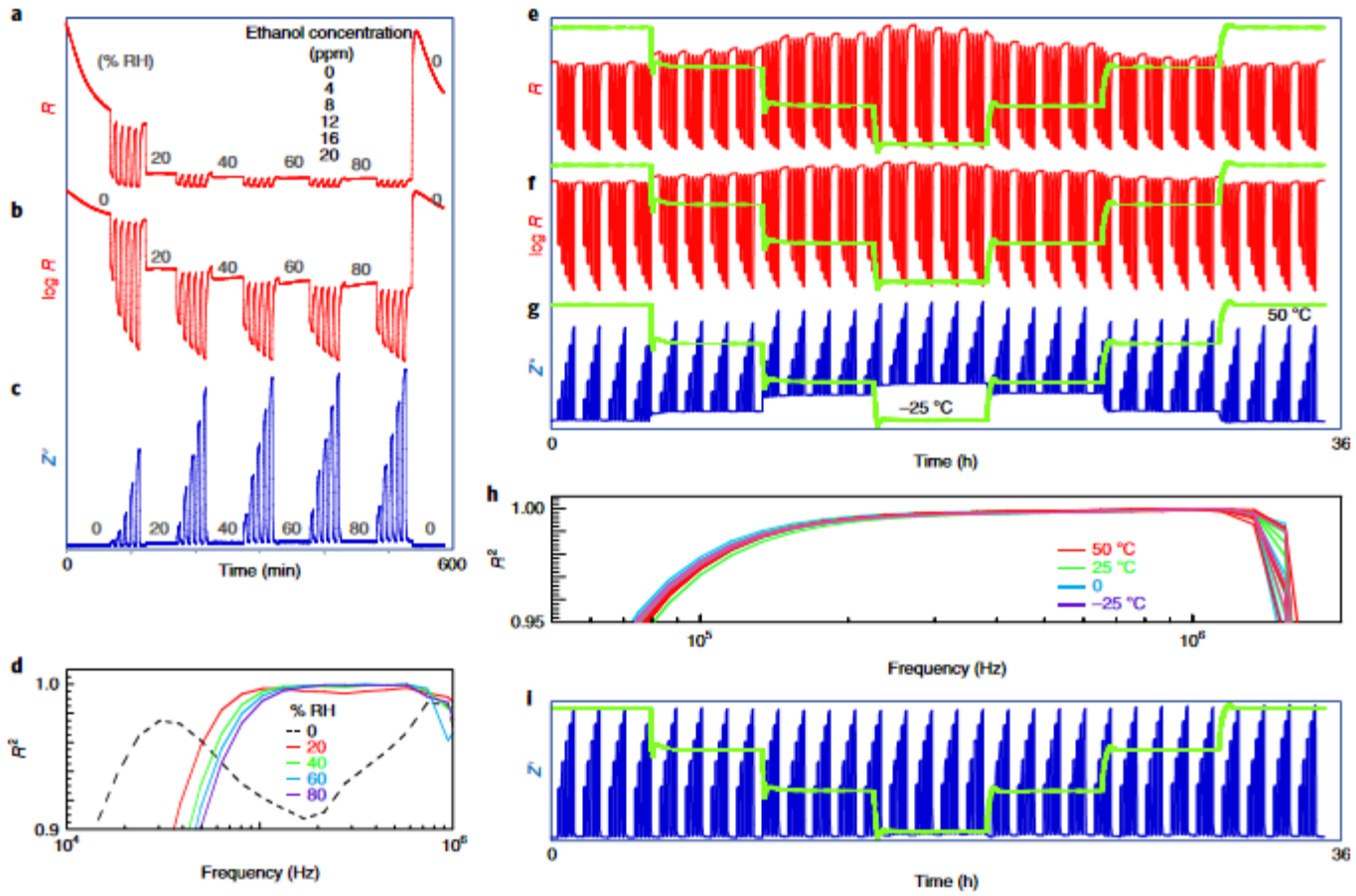

Fig. 3 | Effects of ambient humidity and temperature on the resistance and dielectric responses of SMOX sensing elements. a–d, Effects of ambient humidity from 0 to 80% RH on exposures to ethanol vapour on the resistance response, linear scale (**a**), resistance response, logarithmic scale (**b**) and dielectric response (Z'' at 0.17 MHz) with a dramatic reduction in the RH effects (**c**), and the frequency dependence of R^2 values of the linear fit for different RH levels (**d**). **e–i**, Effects of ambient temperature from −25 to 50 °C on exposures to methane gas on the resistance response, linear scale (**e**), resistance response, logarithmic scale (**f**) and dielectric response (Z'' at 0.56 MHz) (**g**), frequency dependence of the R^2 values of the linear fit for different ambient temperatures (**h**) and temperature-insensitive dielectric response (Z' at 2.7 MHz) (**i**). **a–d**, Experimental details: sensing element CCS801, ethanol at 0, 4, 8, 12, 16 and 20 ppm and water vapour at 0, 20, 40, 60 and 80% RH. **e–i**, Experimental details: sensing element TGS2611, methane at 0, 50, 100, 150, 200 and 250 ppm and ambient temperature at 50, 25, 0 and −25 °C, as indicated with green lines in **e–g** and **i**.

an elegant solution for self-compensation against a variable ambient temperature. We tested sensors in an environmental chamber with cycling of the ambient temperature from −25 to 50 °C and replicate gas exposures (Fig. 3e–i). The resistance response had the expected ambient-temperature-induced baseline offsets and variable non-linear response (Fig. 3e,f for the linear and logarithmic y scales, respectively). The Z'' sensor response also had ambient-temperature-induced baseline offsets, but with the sensor response linearity preserved at all the tested temperatures with well-behaved baseline steps, for example, as shown in Fig. 3g at 0.56 MHz. The results of the analysis of sensor linearity as R^2 values of the linear fit for all the temperatures (Fig. 3h) showed $R^2 > 0.999$ with a stable frequency range of the linear response.

Interestingly, in this experiment we also found that the real part Z' of the impedance response at 2.7 MHz was not affected by temperature (Fig. 3i). This temperature self-compensation effect is probably a result of the differences in the frequency-controlled temperature dependence of dielectric properties of electrical sensor circuit components (for example, sensing material, substrate and electrodes). Systems components with different temperature coefficients have been implemented previously to eliminate temperature sensitivity in electronic devices whereby at certain operation conditions the components cancel out the overall temperature effects for the whole system[34]. Compensation of the temperature effects on sensor performance typically requires an additional hardware solution[35,36].

Initial design rules for high-linearity SMOX sensors

To develop the initial design rules for high-linearity SMOX sensors, we combined our accumulated experimental knowledge on the response linearity under diverse ambient conditions with the insights from the Nyquist plots from numerous designs of SMOX sensing elements and with the knowledge of the origins of the coefficients K_{gas} and β in equation (3). The non-linear response in chemiresistors is controlled by these two coefficients that aggregate all the sensor design, manufacturing and application-specific variables. In previous studies, the values of these coefficients under the explored ambient conditions were $K_{gas}=0.001–0.1$ and $\beta=0.2–1$ (refs. [13–20]).

To evaluate the effects of K_{gas} and β on the linearity of sensor response with dielectric excitation, we numerically explored the effects of K_{gas} and β on the $Z(f)''$ spectra (equation (2) with gas-modulated resistance, as described by equation (3). As shown in Supplementary Fig. 16, the coefficient K_{gas} controlled the frequency

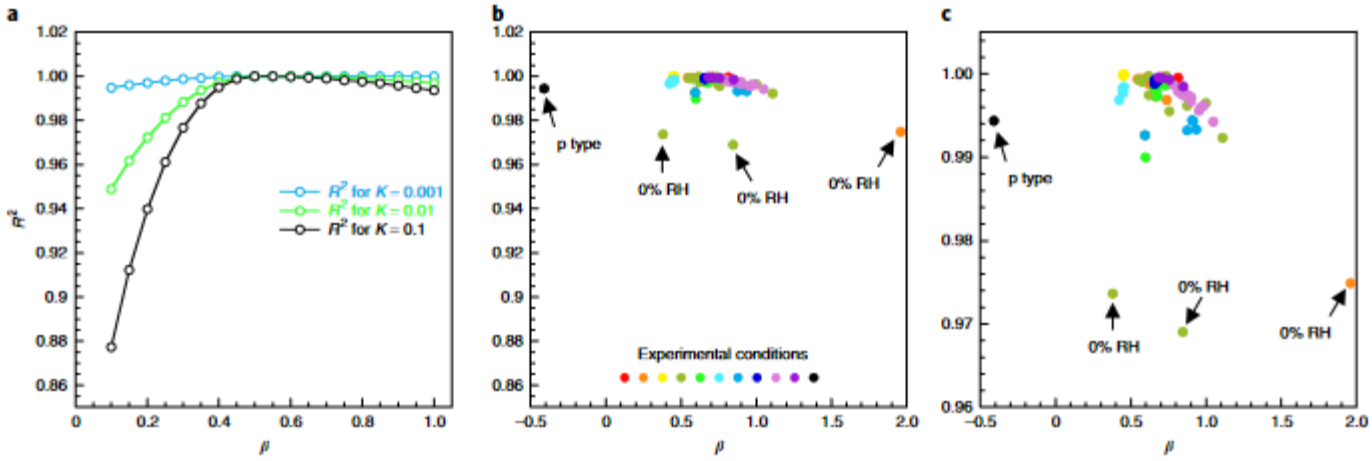

Fig. 4 | Linearity of SMOX gas sensors under dielectric excitation. a–c, Theoretical (**a**) and experimental (**b**,**c**) effects of β and K_{gas} on R^2. In **b** and **c**, we plot experimental data from 70 experimental conditions with 16 types of sensing elements (see Supplementary Table 2 for details). Plot in **c** is the zoomed-in *y* axis of plot in **b**.

region for the highest R^2; the maximum R^2 of 1.00 was achieved for $\beta = 0.5$, which makes this β value the best for the sensor linearity. The highest K_{gas} had the strongest effect on R^2 for different values of β. When β increased from 0.5 to 1, the sensor linearity slightly dropped down to $R^2 = 0.994$ ($K_{gas} = 0.1$). A more important undesired effect of β on the sensor linearity was that when β decreased from 0.5 to 0.1, the sensor linearity dropped down to $R^2 = 0.88$ ($K_{gas} = 0.1$), as summarized in Fig. 4a.

To initially validate this theoretical finding, we performed experiments with 16 sensing elements (n and p type; Supplementary Table 1) and 10 volatiles with their different concentration ranges, mixtures with water vapour up to 80% RH and variation of ambient temperature from −25 to 50 °C. Supplementary Table 2 provides a summary from these experiments with 70 test conditions. Figure 4b,c summarizes the relation between β and R^2 from these experiments, which validates our theoretical predictions. In these figures, we also highlight the p-type SMOX material that has an R^2 value on a par with the values from diverse n-type sensing elements and three R^2 values at $R^2 \approx 0.97$ that were from several experiments in dry air.

Thus, the mechanism of linear gas response at the gas-modulated front shoulder of the relaxation peak in SMOX sensing materials may originate from two aspects. First, Kramers–Kronig relations between the real and imaginary parts of the complex permittivity of diverse types of materials—which include SMOX sensing materials—provide the basis for the correlation between the gas-induced material effects as the d.c. resistance and as the dielectric responses of $Z'(f)$ and $Z''(f)$ under an applied a.c. field[37]. Second, although the $Z'(f)$ gas response is proportional to the power-law dependence under an applied d.c. excitation ($f \to 0$), the frequency shifts of the relaxation frequency f_o of the relaxation peak and the simultaneous change of the amplitude of the $Z''(f)$ signal create a frequency region in which the $Z''(f)$ changes almost linearly in relation to the gas concentration. These theoretical and experimental findings provide us with the initial design rules for high-linearity SMOX-based sensors in which the sensor linearity of $R^2 \approx 1$ is achieved using our dielectric excitation if the sensor is built with the power-law exponent $\beta \approx 0.5$. The coefficient of sensor sensitivity K_{gas} controls the frequency region for the highest R^2.

Improvement in LOD, stability and dynamic response

The baseline instabilities of SMOX chemiresistors is a serious practical limitation that degrades their limit of gas detection[8]. Our dielectric excitation provides a desired solution to this problem. As an example, Figure 5a,b illustrates replicate ($n = 3$) linear and logarithmic responses of a chemiresistor to different hydrogen gas concentrations in the presence of an unstable baseline. In contrast, the dielectric excitation improved the relative levels of the gas-induced responses versus the baseline instabilities (Fig. 5c,d). This improvement was frequency dependent (Fig. 5e). As a result, the LOD was also frequency dependent (Fig. 5f). The LOD for the H_2 chemiresistor was 10.5 ppm, but improved to 0.18 ppm with $Z''(f)$ measurements at ~0.1 MHz. This 58-fold improvement was achieved without any redesign of the sensing material or electrodes, but rather by applying our dielectric excitation.

Dielectric excitation also provided an elegant approach for baseline corrections using a high-frequency portion of the sensor response. We tested the sensor response to periodic exposures to methane ($n = 22$ cycles) for ~130 hours with increasing and decreasing methane concentrations for up to 11% volume. Sensor responses R and Z'' for a single and multiple cycles of gas exposures are presented in Fig. 5g–j to compare the capabilities of both methods. The single-cycle data showed rapid saturation and baseline instabilities of the resistance response (Fig. 5g), but a linear and baseline stable dielectric response (Fig. 5h). Comparison of the sensor performance over the whole test duration revealed baseline instabilities of the resistance response typical for SMOX materials (Fig. 5i,j for the linear and logarithmic *y* scales, respectively) that were almost eliminated in the dielectric response (Fig. 5k). Interestingly, although the high-frequency tail of the spectrum was not affected by the methane response, it revealed a pure baseline fluctuation (green trace of $Z''(f)$ at 3 MHz (Fig. 5l)), which allows a straightforward two-frequency self-correction of the sensor baseline. Such a baseline correction is mathematically not available in single-output sensors[38,39].

In measurements with different gas concentrations, we observed that the sensor recovery time was faster in the $Z''(f)$ measurement mode relative to that in the $Z'(f)$ measurement mode (Fig. 1g–n). This improvement was achieved because under an a.c. excitation at high frequencies, the sensor speed is related only to the grain boundary effects with the fast a.c. displacing charges, whereas in the chemoresistance mode the sensor speed is governed by the d.c. conductance of multijunctions[25,40]. We performed follow-up experiments that compared sensor operational speed with the dielectric excitation and d.c. resistance readouts. Our initial experiments were performed with methane (Extended Data Fig. 6) followed by experiments with numerous additional gases and vapours measured with n- and p-type sensing elements (Extended Data Figs. 3 and 4). The dielectric excitation consistently provided substantial improvements in the sensor recovery time.

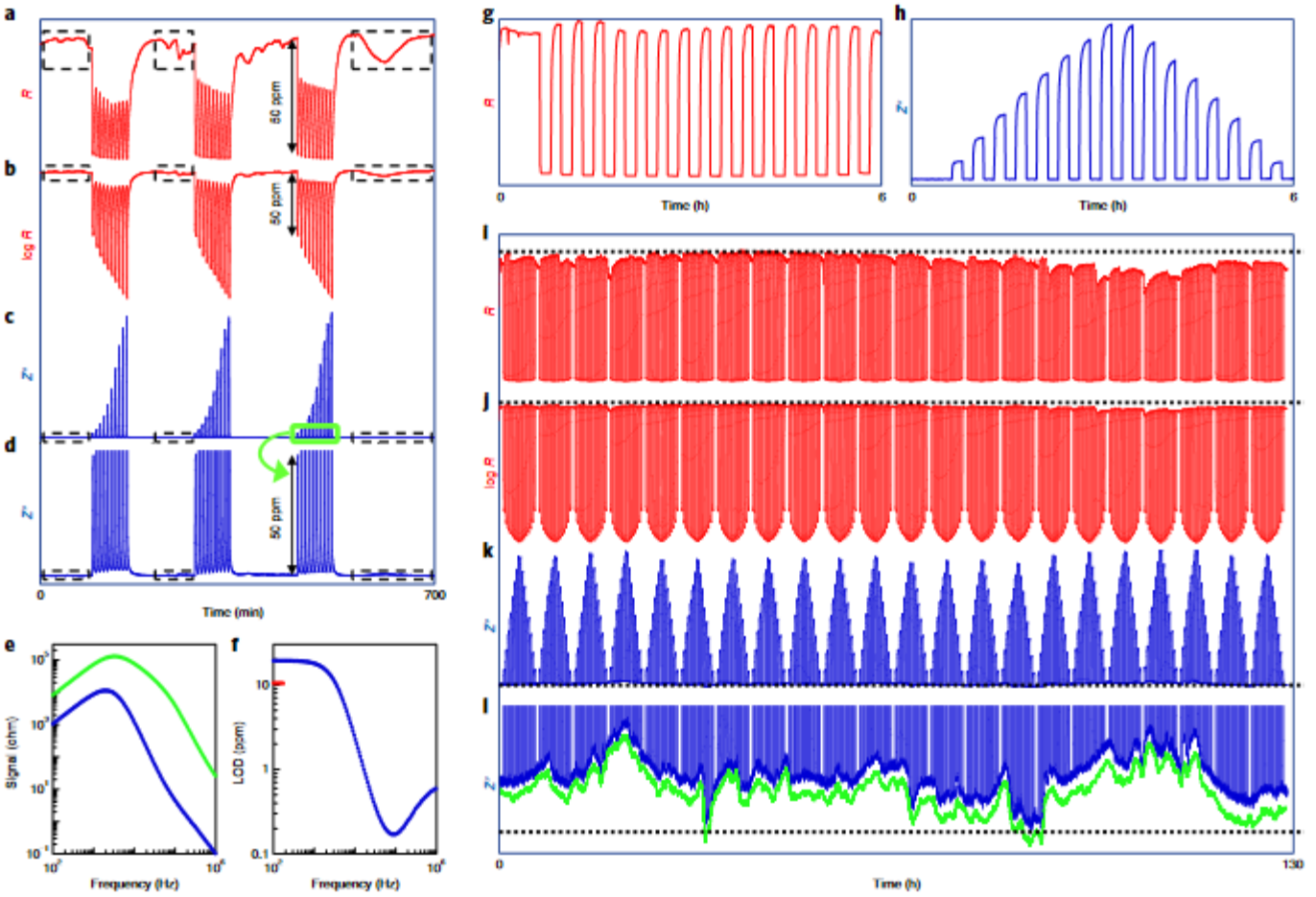

Fig. 5 | General improvement of SMOX sensor baseline using dielectric excitation scheme. a–f, Results of the sensor response to hydrogen concentrations that ranged from 0 to 500 ppm in steps of 50 ppm over the test time of 700 min; sensing element, TGS 821. **a**,**b**, Resistance response on the linear (**a**) and logarithmic (**b**) *y* scales, respectively, depict exemplary large baseline fluctuations (dotted line boxes). **c**,**d**, Z'' response with substantially reduced contributions of the baseline fluctuations (dotted line boxes). Plot in **d** is the zoomed-in *y* axis of plot in **c**. **e**, Frequency-dependent noise of the baseline response (s.d. σ, blue line) and frequency-dependent sensor response to 50 ppm H_2 (green line). **f**, LOD from the $Z''(f)$ response (blue line) illustrates the existence of the minimum in the LOD at ~0.1 MHz with the dielectric excitation, which is ~0.18 ppm of hydrogen, and the LOD from the resistance response of 10.5 ppm (red line). **g–l**, Results of the sensor response to periodic exposures to methane for ~130 h with increasing and decreasing methane concentrations ($n = 22$ cycles). Methane concentrations, 0–11% volume with steps of 1.37% volume; sensing element, TGS 2611. **g**,**h**, Single cycle of resistance (**g**) and dielectric excitation (**h**) responses. **i–k**, Replicate cycles of resistance response on the linear (**i**) and logarithmic (**j**) *y* scales, and dielectric response (Z'' at 0.7 MHz) (**k**). **l**, Zoomed-in regions of the Z'' baseline instability illustrated at 0.7 MHz (blue trace) and 3 MHz (green trace). The blue and green traces are offset for clarity. Black dotted lines in **i–l** show an ideal flat baseline.

Multigas sensing and miniaturization for field deployments

Our main goal was not to focus on multigas detection using a.c. excitation because such a capability was demonstrated earlier[24,39,41]. However, as we had already characterized our available conventional SMOX sensing elements for their response linearity and stability in variable ambient conditions, we also illustrated in this work their capabilities in the discrimination and quantitation of diverse and closely related gases and their mixtures. Supplementary Note 6 and Supplementary Figs. 17–21 summarize our results with gases of importance to environmental pollution (fugitive emissions of methane, ethane and propane), workplace safety (carbon monoxide, methane and hydrogen) and process monitoring (dissolved gas analysis of transformer oils—acetylene, hydrogen and methane). For efficient multigas sensing with future SMOX sensors, their structural designs should be accordingly advanced to provide the required diversity in their independent outputs[38,39].

We further implemented our strategy with commercial integrated-circuit impedance analysers to monitor urban and industrial pollution sources over a broad range of concentrations. Figure 6 compares the results of sensors based on the dielectric excitation for measurements of exemplary volatiles such as benzene, toluene, hydrogen, formaldehyde, and carbon monoxide measured by desktop (top graphs) and integrated circuit (bottom graphs) impedance analysers. Both configurations of the dielectric excitation measurements had similar linearity and ppb LOD values of detected chemical species (summarized in Supplementary Table 3). The advantages of the integrated circuit system were in providing a $>10^3$-fold power reduction and an about 10^6-fold reduction in volume over the desktop impedance analyser.

We also built wireless sensor nodes based on modern low-power microelectronics and employed them for unattended, drone-based and wearable environmental and industrial gas monitoring. The results of these field validation campaigns are presented in Supplementary Notes 7–9, Extended Data Figs. 7–9 and Supplementary Figs. 22–29.

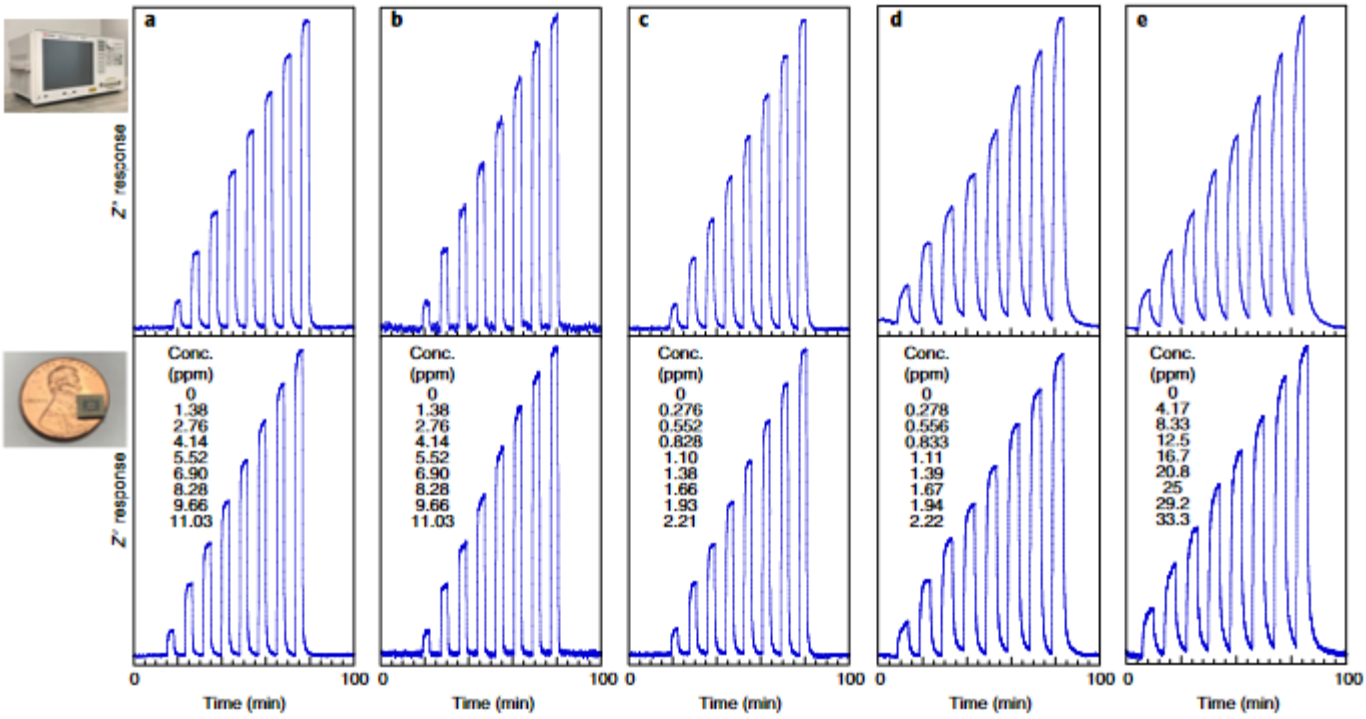

Fig. 6 | Dielectric excitation measurements of responses of SMOX sensing elements to various volatiles with LODs at ppb levels. a–e, Measured chemical species—benzene (**a**), toluene (**b**), hydrogen (**c**), formaldehyde (**d**) and carbon monoxide (**e**)—measured by a desktop (top graphs) and an integrated circuit impedance analyser (bottom graphs). The ppb LOD values are summarized in Supplementary Table 3. Conc, concentration.

Conclusions

We have developed a gas-sensing strategy for conventional SMOX materials that is based on dielectric excitation measurements. The approach offers a linear response, broad dynamic range and baseline stability, as well as substantially reduced humidity and ambient temperature effects. We believe that our dielectric excitation measurement strategy could be easily adapted to a variety of n- and p-type SMOX sensing materials and implemented in a range of emerging applications, which include wearable monitors, autonomous robotics, home health and sensor networks. The broad acceptance of other (physical and physiological) sensors in mobile devices is the guiding force for our gas sensors for indoor air quality and outdoor ambient air quality, toward improving their performance to be on par with traditional analytical instruments[42–44].

SMOX-based sensors could also complement modern miniaturized traditional analytical instruments (such as wearable gas chromatographs[45]) in terms of gas selectivity and accurate detection in complex backgrounds by adopting insights from other areas of analytical instrumentation. For example, SMOX chemiresistors have only a single output, whereas traditional analytical instruments have multiple outputs, because of their different theoretical design origins[38], to enable the accurate quantitation of gaseous chemical species of interest in the presence of known and unknown interferences. The design principles of individual multivariable sensors based on multiresponse sensing materials and transducers that provide up to four-dimensional response dispersion[39,46] and outperform conventional sensor arrays[47] could be considered also. The system-level integration of such ideas could optimize the performance of future SMOX gas sensors in diverse scenarios.

Methods

Sensing elements. The SMOX sensing elements were purchased from different manufacturers; their types and tested gases are summarized in Supplementary Table 1. Where possible, SnO_2 sensing materials were selected as the n-type SMOX materials. As a control, we also used a p-type SMOX material, as highlighted in Supplementary Table 1. The operating temperature of the sensing elements was controlled by the applied voltage of the heater and was typically at 300 °C, as described by the manufacturers. Cross-sectional SEM imaging and energy-dispersive X-ray spectroscopy analysis were performed to explore the morphology and composition of the sensing materials in contact with one of the electrodes. EBAC microscopy was implemented to visualize the conduction paths in the device. The EBAC irradiation conditions for SnO_2 were 10 keV with a 14 nA electron beam.

Exposures to gases and vapours. Different concentrations of gases, vapours and their mixtures were produced using three custom-made computer-controlled gas generation and mixing systems with complementary capabilities, using air as a carrier gas and a total gas flow of ~0.2–1 l min^{-1}. System 1 was operated with non-explosive levels of gases and vapours. System 2 was operated with explosive and highly toxic gases in a walk-in hood. System 3 was operated with non-explosive levels of gases and vapours and was utilized in conjunction with sensor tests in an environmental chamber[47–50].

Sensor data acquisition. The impedance spectra $\bar{Z}(f)$ of sensors were measured using laboratory and ASIC (application-specific integrated circuit) impedance analysers. The laboratory impedance analysers were Agilent 4294A (Agilent Technologies, Inc.) operating from 40 Hz to 110 MHz, Keysight E4990A (Keysight Technologies) operating from 20 Hz to 10 MHz, Keysight E4990A operating from 20 Hz to 20 MHz and Keysight E4990A operating from 20 Hz to 120 MHz. The ASIC impedance analysers were AD5933 and ADuCM355 chips (Analog Devices, Inc.) operating from 1 to 100 kHz and from 1 to 200 kHz, respectively. In laboratory evaluations, data acquisition from desktop analysers and the ASIC analysers was performed using LabVIEW (National Instruments). The sensor nodes were designed to collect data and to send it using Wi-Fi to a central hub where the data was stored in ASCII format and analysed. Examples of the size and power consumption are: Keysight E4990A, 22 cm × 30 cm × 43 cm, ~160 W; ADuCM355, 1 mm × 5 mm × 6 mm, ~50 mW.

Analysis of sensor data. Analysis of sensor data was done using KaleidaGraph (Synergy Software), Python (Python Software Foundation) and PLS_Toolbox Software (Eigenvector Research, Inc.) operated with MATLAB (The Mathworks Inc.). Multivariate data processing was done in MATLAB and Python. Statistical and machine-learning methods were implemented for the qualitative and quantitative analyses.

The support vector machine (SVM) method was used as the supervised learning algorithm that analyses data the for classification and regression analysis. The support vector machine constructs a set of hyperplanes in multidimensional space that is utilized for classification, regression and outlier detection[51].

The principal components analysis (PCA) method was used as an unsupervised method for pattern recognition for the classification of multivariate data. Principal components analysis reduces a multidimensional dataset by calculating orthogonal principal components that are oriented in the direction of the maximum variance within the dataset[52].

A one versus all (OVA) method was used for the classification of measurement results that exhibit a high degree of correlation in variations in the same class. One versus all utilizes training of a single classifier per class, where given a classification problem with N possible solutions, a one-versus-all solution consists of N separate binary classifiers—one binary classifier for each possible outcome[53].

The heat maps depicted in Supplementary Fig. 17e–g were constructed by calculating at each frequency the ratio of the sensor response for a pair of gases and then calculating the magnitude of the difference in this quantity for pairs of frequencies. Mathematically, this is represented for gases 1,2 at a pair of frequencies i,j as:

$$D_{ij} = \left| \frac{Z_i''(\text{gas 2})}{Z_i''(\text{gas 1})} - \frac{Z_j''(\text{gas 2})}{Z_j''(\text{gas 1})} \right|$$

where D_{ij} is the quantity shown in the heat map and $Z_f''(\text{gas } g)$ is the sensor response at frequency f when gas g is present. If the sensor has similar selectivity at frequencies i and j, then $\frac{Z_i''(\text{gas 2})}{Z_i''(\text{gas 1})} \approx \frac{Z_j''(\text{gas 2})}{Z_j''(\text{gas 1})}$ and $D_{ij} \approx 0$. However, if the sensor has different selectivities at frequencies i and j then $\frac{Z_i''(\text{gas 2})}{Z_i''(\text{gas 1})} \neq \frac{Z_j''(\text{gas 2})}{Z_j''(\text{gas 1})}$ and $D_{ij} > 0$. Pairs of frequencies with $D_{ij} > 0$ have diversity in their selectivity and therefore are good candidates to include as independent variables in transfer functions for the independent quantification of different gases using a single sensor.

The LOD was calculated at a signal-to-noise ratio (SNR) of three[54] from the sensor response S at its smallest measured gas concentration and the measured sensor noise σ as $\text{LOD} = \text{SNR} \times \sigma \times [\text{gas}]/S$.

Physics-based gas-leak localization modelling was performed by using ANSYS (Fluent, Inc.), a computational fluid dynamics software package to simulate methane gas leaks into air, which form plumes that evolve under dynamic wind conditions. The developed model solved Naiver–Stokes equations with a k-epsilon submodel for transient flow field simulation, given wind data (wind speed and direction, from a weather station) and ppm methane gas concentrations monitored by the wireless sensor nodes as the inputs. A methane-transport submodel was used for gas-leak tracking, and probing points were defined to capture the methane leak concentrations at various locations. The model was run with various leak locations. For each leak location, the resulting responses at the probing points after running the model were compared with the actual responses from the sensor nodes. Then, the candidate leak location with the best match was determined as the predicted leak location by the model. After the leak location was determined, the leak rate was quantified by further postprocessing of the responses of the model and actual field testing.

Data availability

The data that support the plots within this paper and other findings of this study are available from the corresponding author upon reasonable request.

Received: 11 June 2019; Accepted: 25 March 2020;
Published online: 11 May 2020

References

1. Lewis, A. & Edwards, P. Validate personal air-pollution sensors. *Nature* **535**, 29–31 (2016).
2. Kalantar-Zadeh, K. et al. A human pilot trial of ingestible electronic capsules capable of sensing different gases in the gut. *Nat. Electron.* **1**, 79–87 (2018).
3. Nugroho, F. A. et al. Metal–polymer hybrid nanomaterials for plasmonic ultrafast hydrogen detection. *Nat. Mater.* **18**, 489–495 (2019).
4. van den Broek, J., Abegg, S., Pratsinis, S. E. & Güntner, A. T. Highly selective detection of methanol over ethanol by a handheld gas sensor. *Nat. Commun.* **10**, 4220 (2019).
5. Tao, N. Challenges and promises of metal oxide nanosensors. *ACS Sens.* **4**, 780–780 (2019).
6. Williams, D. E. Low cost sensor networks: how do we know the data are reliable? *ACS Sens.* **4**, 2558–2565 (2019).
7. Hunter, G. W. et al. Editors' choice—critical review—a critical review of solid state gas sensors. *J. Electrochem. Soc.* **167**, 037570 (2020).
8. Ihokura, K. & Watson, J. *Stannic Oxide Gas Sensor: Principles and Applications* (CRC, 1994).
9. Staerz, A., Suzuki, T., Weimar, U. & Barsan, N. In *Tin Oxide Materials* (ed. Orlandi, M. O.) 345–377 (Elsevier, 2020).
10. Rüffer, D., Hoehne, F. & Bühler, J. New digital metal-oxide (MOx) sensor platform. *Sensors* **18**, 1052 (2018).
11. Finkbeiner, S. *Keynote: How Software Makes MEMS Sensors into Smart Systems* MEMS & Sensors Executive Congress MSEC 2019, San Diego, CA, October 22–24 (MSIG, 2019).
12. Cipriano, D. & Capelli, L. Evolution of electronic noses from research objects to engineered environmental odour monitoring systems: a review of standardization approaches. *Biosensors* **9**, 75 (2019).
13. Clifford, P. K. & Tuma, D. T. Characteristics of semiconductor gas sensors I. Steady state gas response. *Sens. Actuators* **3**, 233–254 (1982).
14. Gurlo, A., Barsan, N., Ivanovskaya, M., Weimar, U. & Göpel, W. In_2O_3 and MoO_3–In_2O_3 thin film semiconductor sensors: interaction with NO_2 and O_3. *Sens. Actuators B* **47**, 92–99 (1998).
15. Barsan, N. & Weimar, U. Conduction model of metal oxide gas sensors. *J. Electroceram.* **7**, 143–167 (2001).
16. Yamazoe, N. & Shimanoe, K. Theory of power laws for semiconductor gas sensors. *Sens. Actuators B* **128**, 566–573 (2008).
17. Tricoli, A., Graf, M. & Pratsinis, S. E. Optimal doping for enhanced SnO_2 sensitivity and thermal stability. *Adv. Funct. Mater.* **18**, 1969–1976 (2008).
18. Kamble, V. B. & Umarji, A. M. Achieving selectivity from the synergistic effect of Cr and Pt activated SnO_2 thin film gas sensors. *Sens. Actuators B* **236**, 208–217 (2016).
19. Hua, Z., Li, Y., Zeng, Y. & Wu, Y. A theoretical investigation of the power-law response of metal oxide semiconductor gas sensors I: Schottky barrier control. *Sens. Actuators B* **255**, 1911–1919 (2018).
20. Urasinska-Wojcik, B. & Gardner, J. W. H_2S sensing in dry and humid H_2 environment with p-type CuO thick-film gas sensors. *IEEE Sens. J.* **18**, 3502–3508 (2018).
21. Izawa, K., Ulmer, H., Staerz, A., Weimar, U. & Barsan, N. In *Gas Sensors Based on Conducting Metal Oxides: Basic Understanding, Technology and Applications* (eds Barsan, N. & Schierbaum, K.) 217–257 (Elsevier, 2019).
22. Degler, D., Weimar, U. & Barsan, N. Current understanding of the fundamental mechanisms of doped and loaded semiconducting metal oxide-based gas sensing materials. *ACS Sens.* **4**, 2228–2249 (2019).
23. Ngai, K. L., Jonscher, A. K. & White, C. T. On the origin of the universal dielectric response in condensed matter. *Nature* **277**, 185–189 (1979).
24. Weimar, U. & Göpel, W. A. C. Measurements on tin oxide sensors to improve selectivities and sensitivities. *Sens. Actuators B* **26**, 13–18 (1995).
25. Bueno, P. R., Varela, J. A. & Longo, E. Admittance and dielectric spectroscopy of polycrystalline semiconductors. *J. Eur. Ceram. Soc.* **27**, 4313–4320 (2007).
26. Su, Y. et al. Pd-loaded SnO_2 hierarchical nanospheres for a high dynamic range H_2S microsensor. *RSC Adv.* **9**, 5987–5994 (2019).
27. Chakraborty, S., Sen, A. & Maiti, H. S. Complex plane impedance plot as a figure of merit for tin dioxide-based methane sensors. *Sens. Actuators B* **119**, 431–434 (2006).
28. Barsan, N. & Weimar, U. Understanding the fundamental principles of metal oxide based gas sensors; the example of CO sensing with SnO_2 sensors in the presence of humidity. *J. Phys. Condens. Matter* **15**, R813–R839 (2003).
29. Wicker, S., Guiltat, M., Weimar, U., Hémeryck, A. & Barsan, N. Ambient humidity influence on CO detection with SnO_2 gas sensing materials. A combined DRIFTS/DFT investigation. *J. Phys. Chem. C* **121**, 25064–25073 (2017).
30. Zhu, H. et al. A new insight into cross-sensitivity to humidity of SnO_2 sensor. *Small* **14**, 1703974 (2018).
31. Wang, J. et al. The effect of humidity on the dielectric properties of (In + Nb) co-doped SnO_2 ceramics. *J. Eur. Ceram. Soc.* **39**, 323–329 (2019).
32. Mallires, K. R., Wang, D., Tipparaju, V. V. & Tao, N. Developing a low-cost wearable personal exposure monitor for studying respiratory diseases using metal oxide sensors. *IEEE Sens. J.* **19**, 8252–8261 (2019).
33. Collier-Oxandale, A. M., Thorson, J., Halliday, H., Milford, J. & Hannigan, M. Understanding the ability of low-cost MOx sensors to quantify ambient VOCs. *Atmos. Meas. Tech.* **12**, 1441–1460 (2019).
34. Li, W., Short, J. D. & Possin, G. E. Apparatus for reducing photodiode thermal gain coefficient. US patent 8,564,086 (2013).
35. Vlasov, Y., Green, W. M. & Xia, F. High-throughput silicon nanophotonic wavelength-insensitive switch for on-chip optical networks. *Nat. Photon.* **2**, 242–246 (2008).
36. Middlemiss, R. et al. Measurement of the earth tides with a MEMS gravimeter. *Nature* **531**, 614–617 (2016).
37. Jonscher, A. K. Physical basis of dielectric loss. *Nature* **253**, 717–719 (1975).
38. Booksh, K. S. & Kowalski, B. R. Theory of analytical chemistry. *Anal. Chem.* **66**, 782A–791A (1994).
39. Potyrailo, R. A. Multivariable sensors for ubiquitous monitoring of gases in the era of internet of things and industrial internet. *Chem. Rev.* **116**, 11877–11923 (2016).
40. Schipani, F. et al. Electrical characterization of semiconductor oxide-based gas sensors using impedance spectroscopy: a review. *Rev. Adv. Sci. Eng.* **5**, 86–105 (2016).

41. Schierbaum, K. D., Weimar, U. & Göpel, W. Multicomponent gas analysis: an analytical chemistry approach applied to modified SnO_2 sensors. *Sens. Actuators B* **2**, 71–78 (1990).
42. Gilliam, J. H. & Hall, E. S. *Reference and Equivalent Methods Used to Measure National Ambient Air Quality Standards (NAAQS) Criteria Air Pollutants* Vol. I EPA/600/R-16/139 (US EPA Office of Research and Development National Exposure Research Laboratory, 2016).
43. Lewis, A. C., von Schneidemesser, E. & Peltier, R. E. *Low-Cost Sensors for the Measurement of Atmospheric Composition: Overview of Topic and Future Applications* WMO no. 1215 (World Meteorological Organization, 2018).
44. Fortenberry, C. et al. Analysis of indoor particles and gases and their evolution with natural ventilation. *Indoor Air* **29**, 761–779 (2019).
45. Wang, J. et al. Belt-mounted micro-gas-chromatograph prototype for determining personal exposures to volatile-organic-compound mixture components. *Anal. Chem.* **91**, 4747–4754 (2019).
46. Potyrailo, R. A. Toward high value sensing: monolayer-protected metal nanoparticles in multivariable gas and vapor sensors. *Chem. Soc. Rev.* **46**, 5311–5346 (2017).
47. Potyrailo, R. A. et al. Towards outperforming conventional sensor arrays with fabricated individual photonic vapour sensors inspired by *Morpho* butterflies. *Nat. Commun.* **6**, 7959 (2015).
48. Potyrailo, R. A. et al. Discovery of the surface polarity gradient on iridescent *Morpho* butterfly scales reveals a mechanism of their selective vapor response. *Proc. Natl Acad. Sci. USA* **110**, 15567–15572 (2013).
49. Potyrailo, R. A., Karker, N., Carpenter, M. A. & Minnick, A. Multivariable bio-inspired photonic sensors for non-condensable gases. *J. Opt.* **20**, 024006 (2018).
50. Potyrailo, R. A. et al. Multi-gas sensors for enhanced reliability of SOFC operation. *ECS Trans.* **91**, 319–328 (2019).
51. Cortes, C. & Vapnik, V. Support-vector networks. *Mach. Learn.* **20**, 273–297 (1995).
52. Martens, H. & Martens, M. *Multivariate Analysis of Quality. An Introduction* (Wiley, 2001).
53. Rifkin, R. & Klautau, A. In defense of one-vs-all classification. *J. Mach. Learn. Res.* **5**, 101–141 (2004).
54. Ingle, J. D. Jr & Crouch, S. R. *Spectrochemical Analysis* (Prentice Hall 1988).

Acknowledgements

Different phases of this project were funded by GE Research Innovation Fund, GE Services, National Institute for Occupational Safety and Health Contracts 211-2015-63806 and 75D30118C02617, GE Renewable Energy and BHGE. The findings and conclusions in this study should not be construed to represent any determination or policy of the US Government. The content of this report does not necessarily reflect the position or the policy of the US Government. Certain commercial equipment, instruments or materials are identified in this paper to foster understanding. Such identification does not imply recommendation or endorsement by the National Institute for Occupational Safety and Health and the National Institute of Standards and Technology, nor does it imply that the materials or equipment identified are necessarily the best available for the purpose.

Author contributions

R.A.P. conceived and led the research, R.A.P., C.C. and N.A. designed the laboratory and field experiments, R.A.P., S.G., B.A. and R.S.-P. developed the experimental set-ups for the laboratory tests, S.G., D.S., B.A. and R.S.-P. designed the wireless sensor nodes, A.K. designed and performed the nanocharacterization experiments, R.A.P., S.G., N.A., D.E., C.M. and P.M. performed laboratory and field experiments, X.L. and C.C.-D. performed the theoretical modelling, M.N., G.W. and R.A.P. analysed field data from the sensor nodes, R.A.P. and B.S. analysed data from the multigas experiments and R.A.P. wrote the manuscript with input and comments from all the authors.

Competing interests

The authors declare no competing interests.

Additional information

Extended data is available for this paper at https://doi.org/10.1038/s41928-020-0402-3.

Supplementary information is available for this paper at https://doi.org/10.1038/s41928-020-0402-3.

Correspondence and requests for materials should be addressed to R.A.P.

Reprints and permissions information is available at www.nature.com/reprints.

Publisher's note Springer Nature remains neutral with regard to jurisdictional claims in published maps and institutional affiliations.

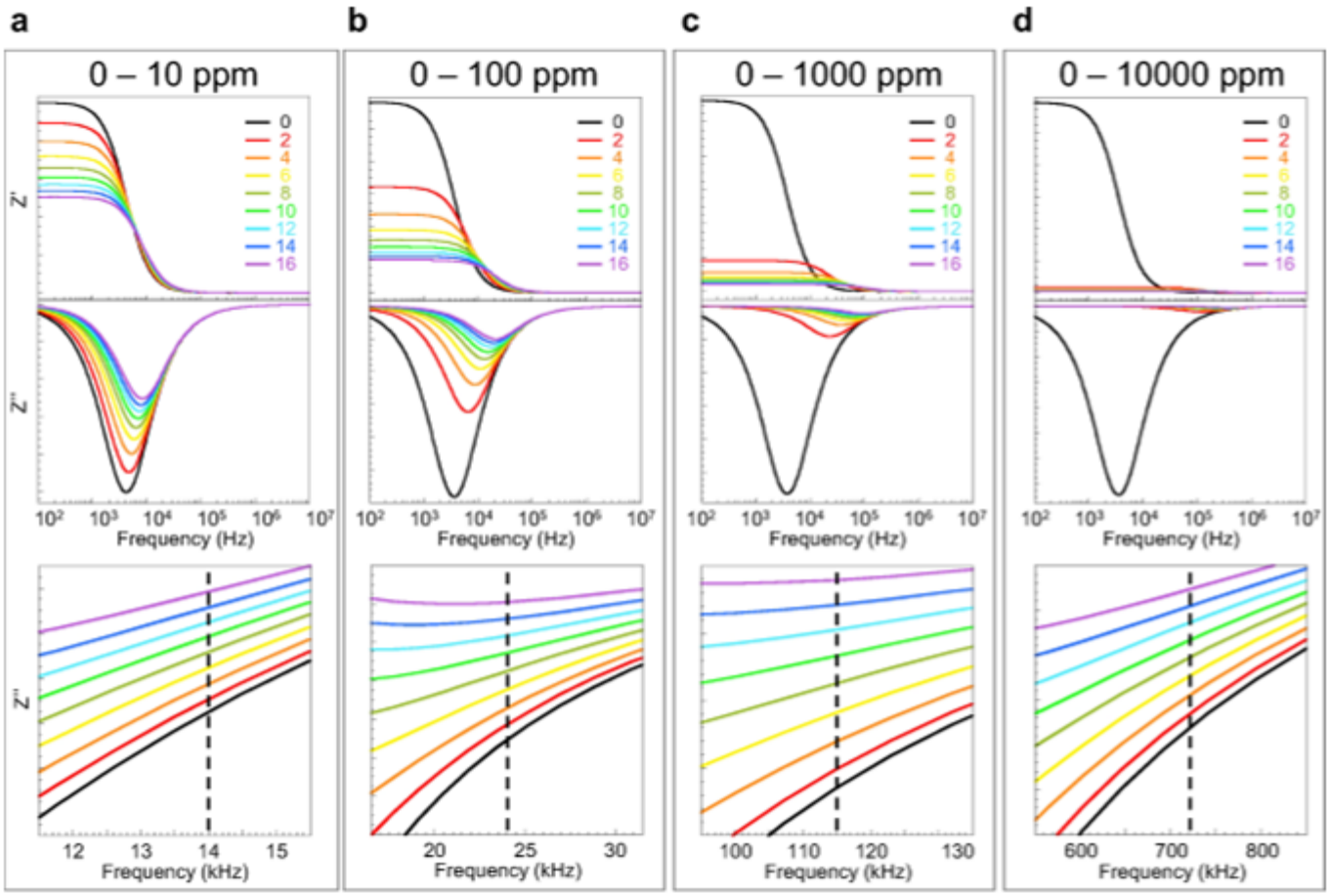

Extended Data Fig. 1 | Spectral details of dielectric excitation measurements of response of a SMOX sensing element to different concentration ranges of methane. a, 0–10 ppm, **b**, 0–100 ppm, **c**, 0–1,000 ppm, and **d**, 0–10,000 ppm. Each panel (**a–d**) has the top graph of $Z'(f)$ spectra, middle graph of $Z''(f)$ spectra and the bottom graph is the zoomed-in region of $Z''(f)$ spectra with the spectral region of the linear sensor response to methane (dotted lines). Different colors in spectra in (**a–d**) are labeled as 0 to 16 as the respective methane gas concentration steps depicted in **Fig. 1g–n** and plotted as a blank (0) and every other spectrum (2–16).

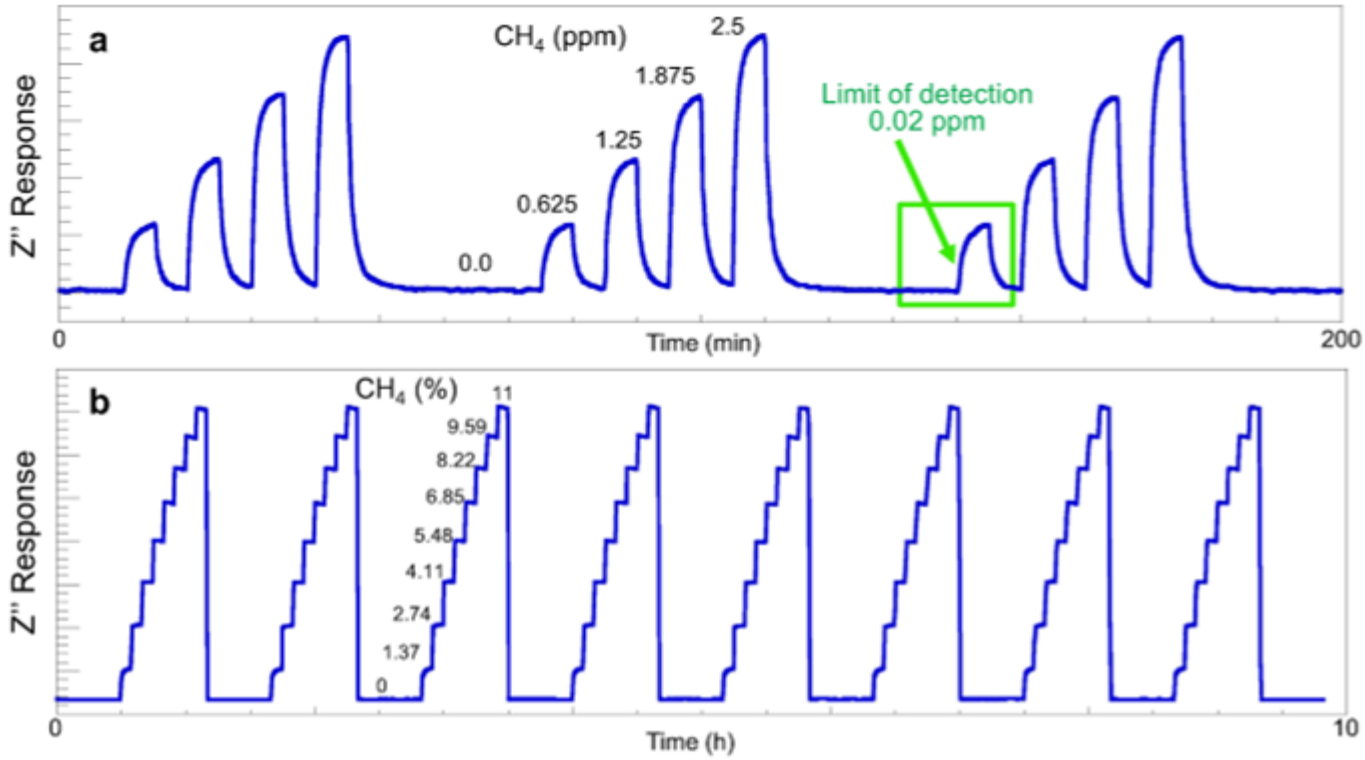

Extended Data Fig. 2 | Broad range of gas-response linearity achieved with dielectric excitation measurements. a, Detection of methane at sub-ppm and low-ppm concentrations with the achieved LOD of 0.02 ppm. **b**, Detection of methane from 0 to 11 % vol.

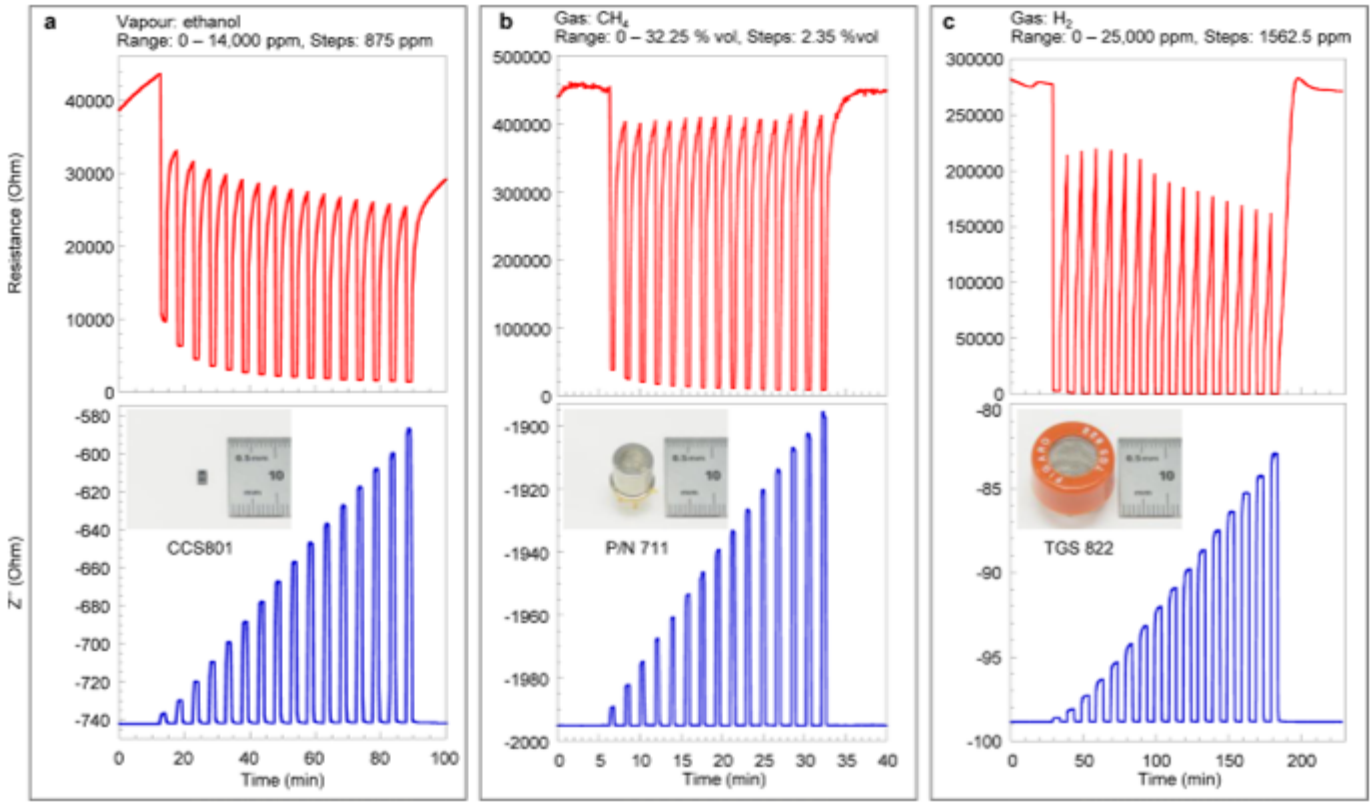

Extended Data Fig. 3 | Examples of responses of different types of SMOX sensing elements to diverse gaseous species obtained using conventional resistance (top graphs) and dielectric excitation measurements (bottom graphs). **a**, Ethanol, **b**, CH_4, **c**, H_2. Insets in bottom graphs are different generations of SMOX sensing elements. For details of the SMOX sensing elements, see Supplementary Table 1. For corresponding Nyquist plots, see Supplementary Fig. 8.